Ionotronic halide perovskite drift-diffusive synapses for low-power neuromorphic computation

John, Rohit Abharam; Yantara, Natalia; Ng, Yan Fong; Narasimmam, Govind; Mosconi, Edoardo; Meggiolaro,Daniele; Kulkarni, Mohit Rameshchandra; Gopalakrishnan, Pradeep Kumar; Nguyen, Chien Anh; De Angelis, Filippo; Mhaisalkar, Subodh Gautam; Basu, Arindam; Mathews, Nripan

2018

John, R. A., Yantara, N., Ng, Y. F., Narasimman, G., Mosconi, E., Meggiolaro, D., ... & Mathews, N. (2018). Ionotronic halide perovskite drift-diffusive synapses for low-power neuromorphic computation. Advanced Materials, 30(51), 1805454-. doi:10.1002/adma.201805454

https://hdl.handle.net/10356/138301

https://doi.org/10.1002/adma.201805454

Ionotronic Halide Perovskite Drift-Diffusive Synapses for Low-Power Neuromorphic Computation

Rohit Abraham John[1], Natalia Yantara[2], Yan Fong Ng[1,2], Govind Narasimman[3], Edoardo Mosconi[4,5], Daniele Meggiolaro[4,5], Mohit R. Kulkarni[1], Pradeep Kumar Gopalakrishnan[3], Nguyen Anh Chien[1], Filippo De Angelis[4,5], Subodh G. Mhaisalkar[1,2], Arindam Basu[3], Nripan Mathews[1,2]*

[1] School of Materials Science and Engineering, Nanyang Technological University, 50 Nanyang Avenue, Singapore 639798

[2] Energy Research Institute @ NTU (ERI@N), Nanyang Technological University, 50 Nanyang Drive, Singapore 637553

[3] School of Electrical and Electronic Engineering, Nanyang Technological University, 50 Nanyang Avenue, Singapore 639798

[4] Computational Laboratory for Hybrid/Organic Photovoltaics (CLHYO), CNR-ISTM, Via Elce di Sotto 8, Perugia I-06123, Italy

[5] D3-Computation, Istituto Italiano di Tecnologia, Via Morego 30, 16163 Genova, Italy

*Corresponding author

Prof. Nripan Mathews (Email: Nripan@ntu.edu.sg)

Keywords: Halide Perovskite, Neuromorphic Computing, Synaptic Plasticity, Ionic semiconductor, Ion migration

Abstract

Emulation of brain-like signal processing is the foundation for development of efficient learning circuitry, but few devices offer the tunable conductance range necessary for mimicking spatiotemporal plasticity in biological synapses. An ionic semiconductor which couples electronic transitions with drift-diffusive ionic kinetics would enable energy-efficient analog-like switching of metastable conductance-states. Here, we utilize ionic-electronic coupling in halide perovskite semiconductors to create memristive synapses with a dynamic continuous transition of conductance-states. Co-existence of carrier injection barriers and ion migration in the perovskite films defines the degree of synaptic plasticity, more notable for the larger organic ammonium and formamidinium cations than the inorganic cesium counterpart. Optimized pulsing schemes facilitates a balanced interplay of short and long-term plasticity rules like paired-pulse facilitation and spike-time dependent plasticity, cardinal for learning and computing. Trained as a memory array, halide perovskite synapses demonstrate reconfigurability, learning, forgetting and fault tolerance analogous to the human brain. Network-level simulations of unsupervised learning of handwritten digit images utilizing experimentally derived device parameters, validates the utility of these memristors for energy-efficient neuromorphic computation, paving way for novel ionotronic neuromorphic architectures with halide perovskites as the active material.

Introduction

Combining computational power in the order of exa-FLOPS and a low power consumption of 20 W, human brain sets the benchmark for computational capability and power efficiency. Comprehensive emulation of neural signatures requires devices with a wide dynamic range of conductance and retention.[1] Synaptic emulation by conventional silicon circuitry often requires additional analog converters, imposing issues with scalability and power consumption.[2–5] Development of next-generation materials and devices for neuromorphic electronics entails detailed understanding of the fundamental device characteristics and their possible emulation capabilities at

an elemental level. Ionically-gated transistors harness diffusive mechanics to achieve continuous modulation of channel conductance at low-power, but require coupling of two disparate electronically- and ionically-active material sets.[6,7] Solutions based on drift-memristors are inherently disadvantaged due to digital-like abrupt switching transitions, which limit their plasticity[8]. Very recently, second-order drift memristors[9,10], electrochemical metallization cells[11] and diffusive memristors[8] have been engineered to approximate the biological Ca^{2+} dynamics based on metal atom diffusion, thermal dissipation[9], mobility decay[12] and spontaneous nanoparticle formation, but often require additional non-volatile elements in series for long-term memory storage. An ionic semiconductor which intimately combines rapid electronic transitions with slow drift-diffusive ionic kinetics will enable dynamic tuning of metastable memristive conductance-states, allowing efficient emulation of synaptic characteristics and catering for novel low-power architectures that exploit electronic properties of the semiconductor.

Halide perovskites are facilely processable ionic semiconductors which have revolutionized the field of photovoltaics and light-emitting diodes (LEDs) with their superior electronic properties, such as long carrier-diffusion lengths and low defect-densities.[13] Ionic effects have been accounted for the origin of hysteresis, slow photocurrent decay as well as above bandgap photo-voltages in perovskite devices.[14–17] These ionic effects co-exist with excellent electronic properties such as low carrier effective mass and high photoluminescence quantum yield enabling construction of high performance solar cells and LEDs.[18] Herein, the memristive signatures due to intimate electronic-ionic coupling in halide perovskites (namely $CH_3NH_3PbBr_3$ ($MAPbBr_3$), $CH(NH_2)_2PbBr_3$ ($FAPbBr_3$) and $CsPbBr_3$) are harnessed to build artificial synapses with concurrent processing and learning abilities (Figures 1A-B, Supplementary Section-A Figure S1). Ionotronic effects modulate the conductance-state, mimicking intracellular Ca^{2+}-Na^{+}-K^{+} flux changing the synaptic conductance. Charge transport pathways emulate the synaptic cleft and device conductance defines the synaptic weight. Co-existence of ion migration-relaxation kinetics and tunable potential barriers

facilitate comprehensive emulation of synaptic plasticity behaviours at both short and long-time scales, forming the basis of memory and learning. Temporally correlated pre- and post-synaptic action potentials initially create short-term volatile changes in the device conductance/weights, which further consolidates to long-term non-volatile changes upon persistent training. These long-term weight changes are then optimized for depicting halide perovskite memristors as a reconfigurable and trainable memory array. With higher activation energies for ion migration, the weight changes- modulatable via amplitude, polarity, number and temporal correlations of training sequences, are observed to be more profound in organic cation-based halide perovskites. Network-level simulations of unsupervised learning based on experimentally measured device properties illustrate the power of these drift-diffusive memristors for pattern recognition and image classification algorithms, paving way for novel ionotronic neuromorphic architectures with halide perovskites as the active material.

Results

In synapses, action-potentials are transduced into chemical-signals through the release of neurotransmitters, which form the crux of decision making. Correlations between presynaptic activity and extent of post-synaptic membrane polarization result in changes in connection weights- **synaptic plasticity**.[19] Plasticity occurs in the human brain on multiple timescales—while long-term plasticity occurring on a time-scale of several minutes is thought to be the basis of experience-dependent modification of the neural circuit, short-term plasticity occurring on a time-scale of tens of milliseconds is useful for temporal filtering and might have a role in speech processing and working memory.[20]

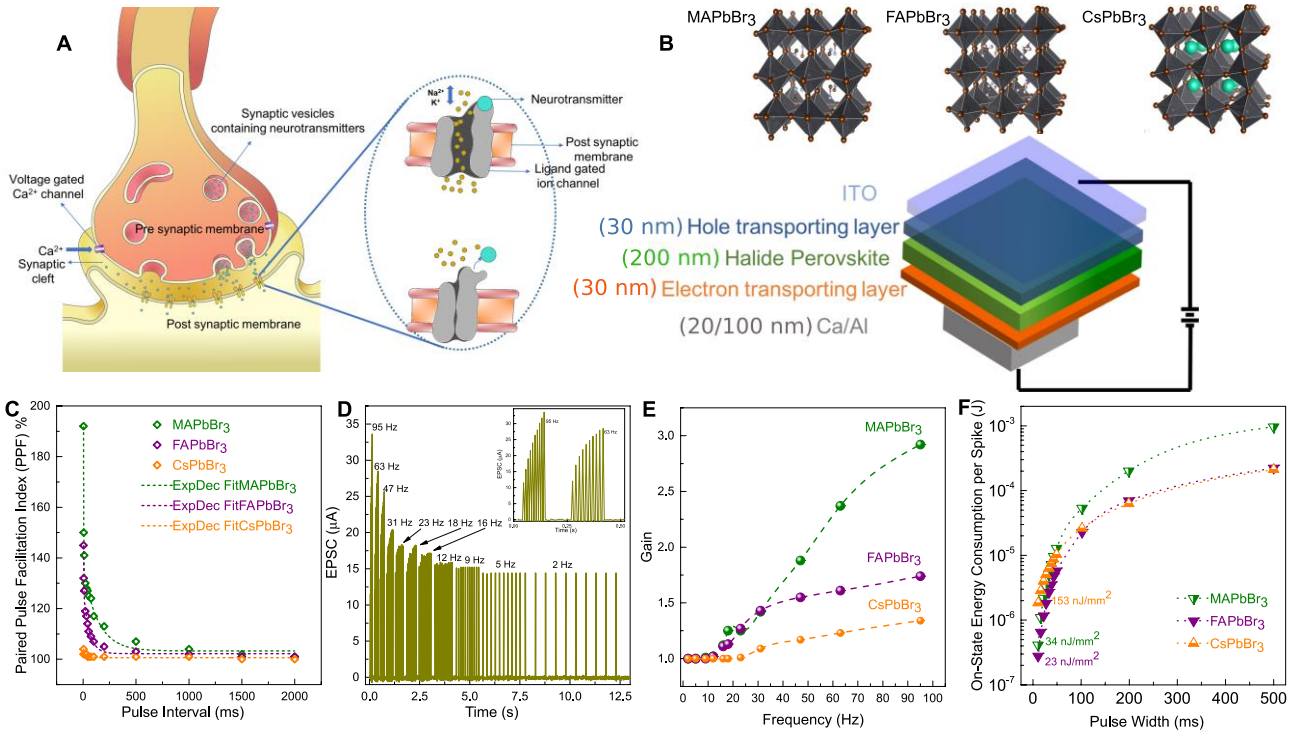

Figure 1. Short-term plasticity features emulated in halide perovskite memristors. (**A**) Schematic of chemical synaptic transmission. Arrival of an action-potential causes selective endocytosis and exocytosis of Na^+, K^+ and Ca^{2+} deciding the extent of membrane polarization. (**B**) Architecture of an artificial synapse with halide perovskites as the active switching materials. Three different materials namely $CH_3NH_3PbBr_3$ ($MAPbBr_3$), $CH(NH_2)_2PbBr_3$ ($FAPbBr_3$) and $CsPbBr_3$ are investigated as switching matrices. The memristive/hysteretic electrical effects in halide perovskites are utilized to create and modulate plasticity in these devices. (**C**) PPF index variation with increasing pulse interval: comparison of $MAPbBr_3$, $FAPbBr_3$ and $CsPbBr_3$. An exponential decay fit is applied to obtain two characteristic timescales as shown in Supplementary Section-B Table T1. All the devices under test depicted diode characteristics with the threshold (V_{th}) for sharp current increase varying from 2 to 2.5 V. Hence for a fair comparison between the three systems and not compromising on the energy consumption per spike, pre-conditioning pulses of + 3 V (> V_{th}) were chosen to simulate short-term plasticity. (**D**) Temporal high-pass filters enabled by frequency-dependent short-term plasticity of halide perovskite memristors. EPSCs in response to presynaptic stimuli trains of different frequencies (2-95 Hz) for MA-based memristors. The stimulus train at each frequency consisted of 10 stimulus spikes of amplitude + 3 V. (**E**) Filter gain (B_{10}/B_1) plotted as a function of pre-synaptic spike frequency. Note: B_{10} and B_1 are amplitudes of the 1st and 10th EPSC for each frequency as shown in (**D**). (**F**) Comparison of the ON-state energy consumption per spike (Eon) of the halide perovskite synapses.

Short-term plasticity evaluation indices such as **Paired-pulse facilitation (PPF)** of all the three devices exceeded 100% with an exponential time-decay behaviour analogous to chemical synapses. Organic cation (MA and FA-based) systems depicted a higher retention and much slower decay when compared to inorganic Cs, and showed an exponential behaviour in resemblance to the coupling of the neurons.[21] At the shortest interval of 5.3 ms, MA-systems exhibited the highest PPF index (192%), as compared to 145 % for FA and 104 % for Cs-devices. This ratio continued to decrease with increasing pulse interval and finally reached around 100 % for the largest pulse interval of 2000 ms (Figure 1C, Supplementary Section-B Figure S2). This observed decay

resembled the coupling of biological neurons and could be fitted with an exponential decay equation.[21,22]

$$y = B_1 * \exp\left(-\frac{x}{t_1}\right) + B_2 * \exp\left(-\frac{x}{t_2}\right) + y_0$$

where x is pulse interval time, y_0 is resting facilitation magnitude, B_1 & B_2 are facilitation constants, and t_1 and t_2 are characteristic time constants of the rapid and slow phases respectively (Supplementary Section-B Table T1). The extracted rapid (t_1) and slow (t_2) time constants were comparable with the time scales previously reported for both emulated[23] (25 ms) and biological systems[24] (40-300 ms). Extending this concept, a training sequence consisting of 10 presynaptic action potentials induced dynamic high-pass temporal filtering[25] of signals via volatile changes in conductance with a frequency-dependent gain (Figures 1 D-E). Slower relaxation time-constants of the organic-cation based perovskites resulted in superior facilitation and thus larger filter gains ($MAPbBr_3$ = 2.92, $FAPbBr_3$ = 1.74 at 95 Hz) when compared to the inorganic Cs-based system ($CsPbBr_3$ = 1.34 at 95 Hz).

Extreme **low power consumption** of the human brain (~10 fJ per synaptic event) remains unmatched by any artificial neural network till date. Hence, our devices were benchmarked on power consumption to investigate the feasibility of realizing ultra-low power neuromorphic circuits. All the three systems under investigation depicted energy scaling in a near linear manner across two orders of dimensional magnitude. FA and MA-based synapses outperformed the Cs-counterparts with an ON-state energy consumption of 23 nJ/mm^2 and 34 nJ/mm^2 per event respectively, making them one of the most energy efficient artificial synapses reported till date (Figure 1F, Supplementary Section-C Figure S3, Table T2).

Repeated presynaptic stimulations consolidated the metastable conductance-states to achieve **long-term potentiation (LTP) and depression (LTD)** in congruence with the Atkinson-Shiffrin multistore model (Figure 2A).[26] Dependent on device history, the magnitude of weight changes

could be tuned by the number and amplitude of the presynaptic training spikes (Figures 2 B-G, Supplementary Section-D Figure S4 Table T3), resulting in controlled facilitation/depression in accordance with the quantal and probabilistic neurotransmitter release model.[27] Slower relaxation nature of the organic cations once again resulted in larger weight changes and higher retention of the memory states as depicted by the **Ebbinghaus forgetting curves**. Spaced repetition resulted in softening of the forgetting process, enhancing memory and learning. Trained with 40 pulses of amplitude + 3 V, width 500 ms and interval 5 ms, MA- synapses depicted long-term change in conductance/weight equivalent to 24.32 %, followed by FA and Cs with 18.61 % and 5.54 % respectively. The degree of long-term weight changes also depended heavily on the amplitude of the training pulses. The long-term weight change in MA-synapses increased to 54.19 % from 24.32 % when the amplitude of the training pulses were increased from + 3 V to + 5 V. Similar trend was observed in FA- and Cs-based synapses as shown in Figures 2 B-G.

Temporal correlations between the pre- and postsynaptic spikes created voltage-dependent changes in conductance/weight, establishing four forms of **spike-timing-dependent plasticity (STDP)** rules. A refinement of Hebb's theory, STDP is considered to be the first law of synaptic plasticity and forms the basis of associative learning.[28] Various forms of STDP have been observed in biological synapses and are attributed to different functions regarding to the information processing and storage.[19] Although several investigations report the most common form of asymmetric Hebbian learning rule, most fail to emulate other forms of Hebbian plasticity.[8,29] Here, four different forms of STDP were realized by modifying the shape of the pre-synaptic and post-synaptic spikes, effectively translating timing differences into voltage amplitude differences (Figures 2H-K). Spike patterns corresponding to Supplementary Section-D Figure S5 were applied in our measurements, and the change in conductance (weight) was recorded as a function of the pulse interval between pre- and postsynaptic spikes. Repeated arrival of pre-post or post-pre spike pairs led to resistance changes above the writing threshold in proportion to the voltage and time-

integrated device conductance function ($f(V_{pre}\text{-}V_{post}), t$), where the net voltage on the device at each instant of time (t) is defined by the voltage difference between the pre- and post-spike ($V_{pre}–V_{post}$).[7] Changes in conductance were compared to the initial conductance value to convert the data to percentage weight changes (reading pulses of 0.5 V was utilized for this measurement). The device was then allowed to relax back or erased to the initial conductance state before the next measurement to avoid dependence of previous history. MA- and FA-based systems depicted a higher modulatable STDP function in comparison to Cs, suggesting the possibility of implementing rate coding schemes with varying STDP time windows. Weight changes were predominant at small pulse intervals, and weakened with increase in the interval, reflecting strong temporal correlations between the pre- and postsynaptic spikes. Flipping of the input waveforms resulted in switching from anti-Hebbian to Hebbian rules. The STDP time windows shown here in milli-seconds and weight changes are comparable to biological values[28] and could be further tuned by modulating the width, number and shape of the input spikes.

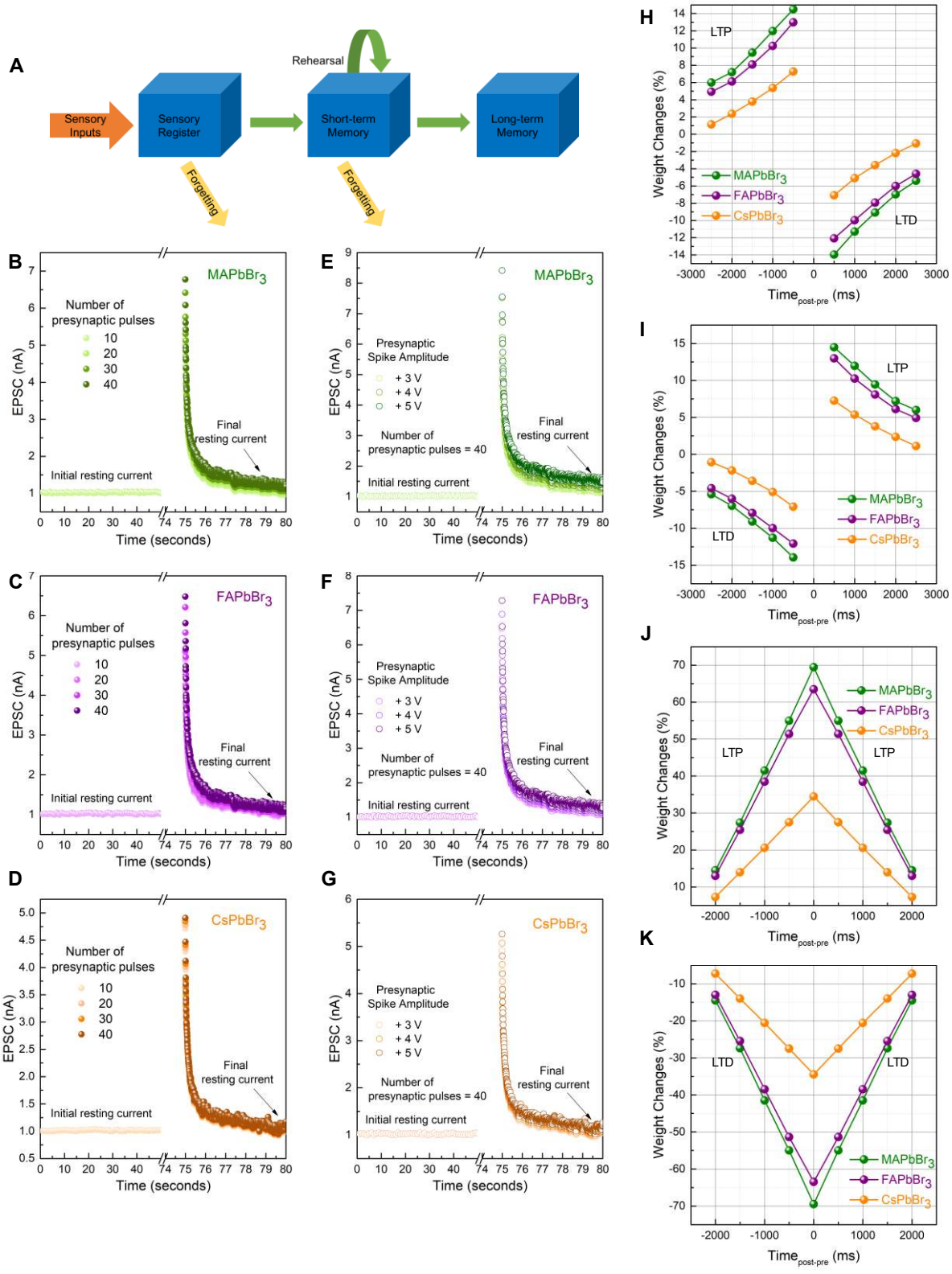

Figure 2. Long-term plasticity in halide perovskite synapses. (**A**) Classification of human memory based on the time scale of retention. Training (**B**) $MAPbBr_3$, (**C**) $FAPbBr_3$ and (**D**) $CsPbBr_3$ synapses with large number of rehearsals resulted in higher weight changes, higher retention and slower decay of memory. Increasing presynaptic pulse amplitudes also resulted in higher weight changes, higher retention and slower decay of memory as indicated by (**E-G**). Hebbian spike-time-dependent plasticity (STDP) variants realized in halide perovskite synapses. Difference in timing of the pre- and post-synaptic pulses are translated into voltage amplitude differences inducing weight changes (ΔW) in the system. Shape of the input waveforms modulated the STDP type and window ranging from (**H**) antisymmetric anti-Hebbian, (**I**) antisymmetric Hebbian, to (**J**) symmetric Hebbian, (**K**) symmetric anti-Hebbian learning rules.

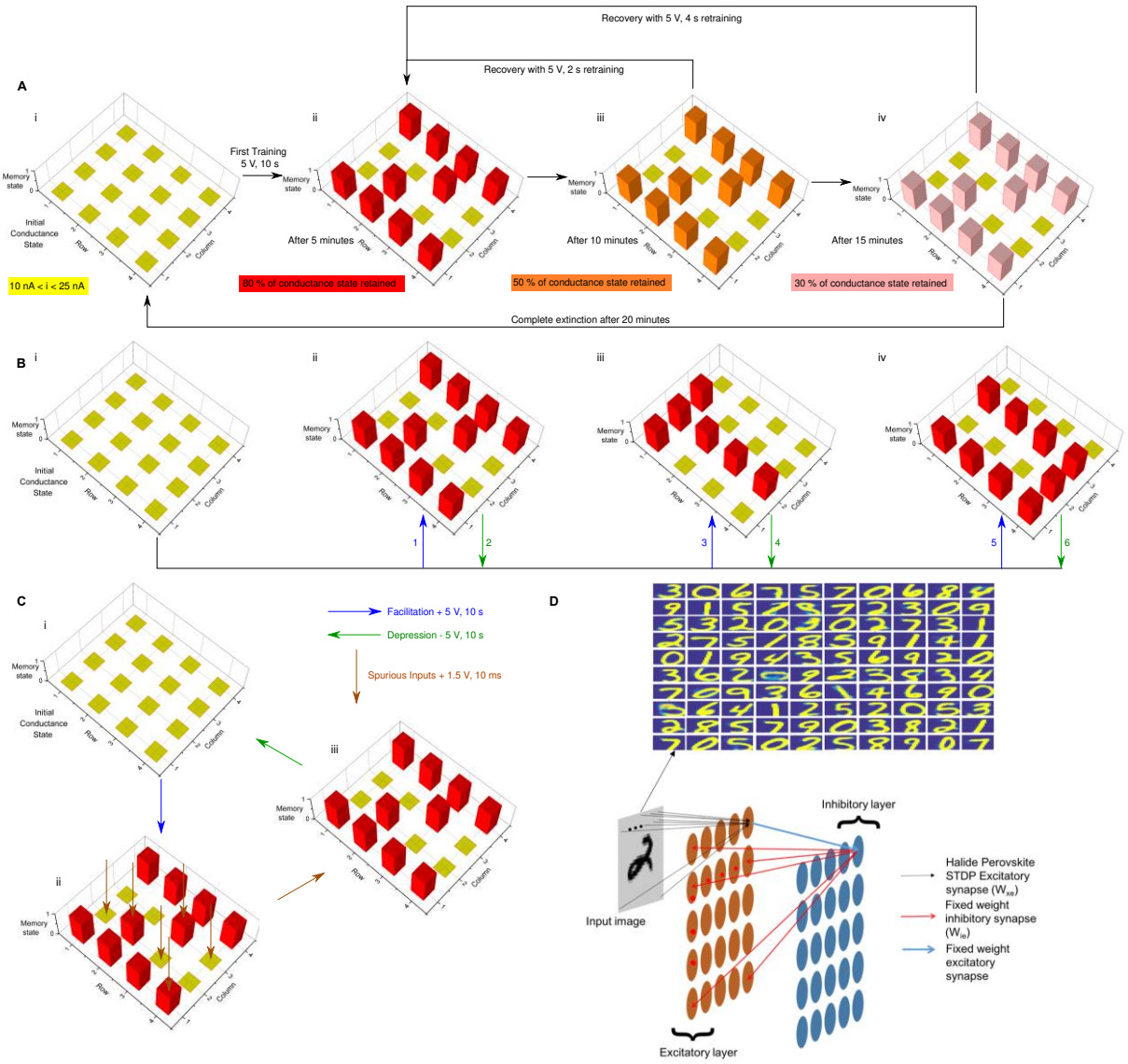

Figure 3. Neuromorphic halide perovskite memory array for pattern recognition. (**A**) A 4x4 array of halide perovskite synapses was implemented as a reconfigurable and trainable memory unit with fault tolerance. The image of "N" was programmed into the array using an external microcontroller biasing (5 V, 10 seconds) individual pixels on demand with others in a floating-mode. With time, these synapses exhibited extinction of memory analogous to forgetting but could be retrained faster to reach the same conductance levels. (**B**) After complete erasing of the image of "N", "T" and "U" were also programmed and erased. (**C**) The memory array also exhibits good fault tolerance and robustness to spurious inputs. Spurious inputs of + 1.5 V, 10 ms did not affect the conductance state on a long time-scale and the pixels could be read successfully. (**D**) The proposed two-layer neural network that is trained in simulations to recognize handwritten digits selected from the MNIST database. All input pixels connect to each excitatory neuron in layer 1 through synapses equipped with STDP behavior. Each excitatory neuron connects to an inhibitory neuron in layer 2 through fixed weight excitatory synapses. Each inhibitory neuron connects to all layer 1 neurons using fixed weight inhibitory synapses inducing winner-take-all based competition among layer 1 neurons. The receptive fields of 100 neurons in the excitatory layer obtained after training on 6000 images are shown here.

To further illustrate the significance of our findings, a 4x4 array employing halide perovskite synapses was experimentally implemented as a **reconfigurable and trainable memory unit with fault tolerance** (Figures 3-A-C). Fresh MA-based synapses were arranged in a pixelated array format with an initial low-conductance state (stage: i). The image of "N" was then programmed into

the array using an external microcontroller that biased (5 V, 10 seconds) selected individual pixels on demand with others in floating-mode. The pixel resistances were then read (+ 0.5 V, 1 second) individually few minutes after the training process and the corresponding readout-conductance map reflected the image of "N". With time, the conductance decreased akin to forgetting in the human brain, but could be retrained with fewer training cycles as shown in stages: ii-iv, reflecting the learning ability of these synapses. After complete extinction of memory of "N" (described procedure in Figure 3A), new patterns corresponding to "T" and "U" were programmed into the same array using facilitating (write) and depressing (erase) pulses as depicted in Figure 3B. Fault tolerance and robustness against non-ideal input signals were then tested by introducing spurious and random spikes (+ 1.5 V, 10 ms width) together with training pulses during the retrain process for the "N" pattern (Figure 3C). The network was seen to remain highly sensitive to the training pulses (re-establishing of memory state) while insensitive to the spurious spikes (no permanent conductance change) at both active ([2,2], [4,1], [3,3]) and non-active ([1,2], [3,2], [4,3]) nodes (Figure 3C). By varying the total writing-erasing time, it is possible to further fine-tune and exploit the wide range of conductance state and memory retention in these devices.

Based on the STDP behaviour of $MAPbBr_3$ synapses (Figure 2I), a two-layer neural network was trained in a simulation to recognize handwritten digits selected from the MNIST database (Supplementary Section-E).[30,31] Input spike trains were connected to the first layer of neurons using synapses initialized with random weights, while the second layer introduced competition within the network by a winner-take-all mechanism.[32] The neuron whose receptive field matched the input pattern best, could further tune its synaptic weights to match the input. Receptive field of neurons in the first layer resembled the handwritten digits after presentation of 6000 images in a randomized order (Figure 3D) through unsupervised learning. Training the neural network using 6000 images resulted in an accuracy of 80.8 %. Compared to other STDP implementations in CMOS[33,34], this approach has the potential of ~ 200X reduction in energy for learning.

Discussion.

Ion migration and charge-trapping effects have been suggested as possible mechanisms for the origin of hysteresis in halide perovskites, leading to slow photocurrent decay, above bandgap photo-voltages and switchable photovoltaic effects.[14–16] Dependent on the local defect structure, energy profile, scanning rate and grain boundaries, these deleterious effects of localized ion redistribution have been studied in detail by various spectroscopic and microscopic investigations.[15,35] The wide variety of synaptic phenomena noted in our devices also support a mechanism of vacancy-mediated ion drift-diffusion, pointing to mixed ionic–electronic conduction in these hybrid perovskites.

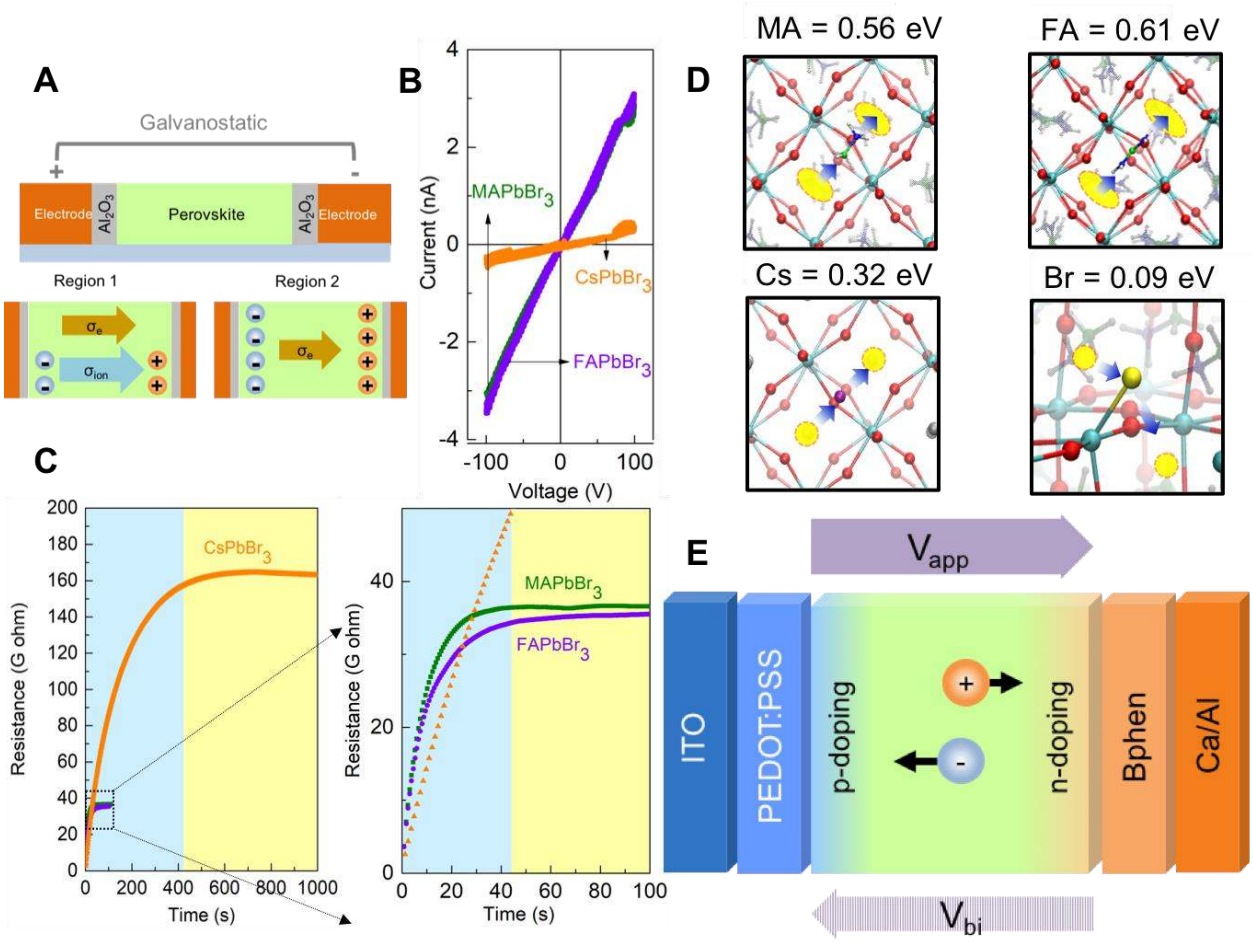

Figure 4. Proposed ionic and electronic conduction in halide perovskites. (A) Galvanostatic measurement setup for ion migration kinetics. Electronic resistance of the films extracted from **(B)** was used to decouple ionic resistance from the total resistance (ionic- blue region and electronic- yellow region) **(C)** for a constant current level. Al_2O_3 (2 nm) was used as an ion blocking layer for this measurement. (**D**) Vacancy-mediated migration-pathways for A-site cations and bromide anions with the calculated activation energies obtained from DFT calculations. (**E**) Schematic of ion migration in halide perovskite synapses. Pulse induced ion redistribution in halide perovskites causes self p- and n-doping and defect passivation, resulting in better carrier injection into the devices. Removal of the bias causes the ions to relax back. This ion migration-relaxation (drift-diffusion) kinetics is modulated by the pre- and post-synaptic training pulse characteristics like amplitude and frequency, to create short and long-term plasticity.

Galvanostatic measurements revealed similar electronic and ionic conductivities for all the three halide perovskite films, reiterating the hybrid electronic-ionic conduction in these systems (Figures 4A-C Supplementary Section-F Table T4). To account for the differences in synaptic signatures observed in the three films and as a first judgement of the kinetics of migrating species, first principles calculations on $MAPbBr_3$, $FAPbBr_3$ and $CsPbBr_3$ were performed on their room-temperature stable phases (pseudo-cubic and orthorhombic, respectively) (Figure 4D Supplementary Section-G Tables T5-6). Our first principles calculations indicated significant differences in vacancy-mediated migration activation energies for A-site cations ($V_{MA\text{-}}$: 0.56 eV, $V_{FA\text{-}}$: 0.61 eV, and $V_{Cs\text{-}}$: 0.32 eV) with their magnitudes indicating a time scale of ~ milli-seconds to minutes. We hypothesize this to be the primary contributing factor of the transient responses noted here since halide motion/relaxation with much lower activation energies are expected to play a role at much faster timescales (< 1 μs).[36] This is consistent with the degree of short and long-term synaptic plasticity observed in our devices which followed the same trend as the vacancy-mediated migration activation energies for the A-site cations.

Therefore, we hypothesize that upon pre-synaptic spike application, negatively charged bromide anions and A-cation vacancies **drift** and accumulate near the hole transporting material interface (self p-doping), while positively charged A-cations and bromide vacancies n-dope the electron transporting material interface (Figure 4E); culminating in better carrier injection.[37] The built-in electric field due to the band alignment between halide perovskites and transport layers and ion concentration gradient result in ion back-**diffusion**/relaxation on bias removal, as also noted in perovskite solar cells.[38] Thus, the carrier injection barrier could be temporarily or persistently regulated, resulting in modulation of device conductance/synaptic weight. In the case of PPF, when the pulse interval was short, ions activated by the first spike do not relax back before application of the second spike. This results in more ions being accumulated near the interfaces, which subsequently reduces the carrier injection barrier, hence increasing the PPF index. Higher PPF

indices indicate slower net ion back-diffusion kinetics which could be attributed to slower cation migration, lower availability of mobile ions, smaller mobile ion formation energy or lower net built-in voltage (V_{bi}) in the organic-cation based systems. Similar film thicknesses, defect formation energies (DFE) (Supplementary Section-G Table T6) and ionic conductivities (Supplementary Section-F Table T4) indicated that a smaller mobile ion formation energy or lower V_{bi} across the organic cation-based system could be responsible for the stronger synaptic response. In addition to perovskite self-doping, ion accumulation at the injection layer interfaces could also modulate the conductivities of the injection layer itself (i.e. both PEDOT: PSS and Bphen).[39] Long-term plasticity (LTP and LTD) could also occur due to permanent pinning of ions at the PEDOT: PSS/perovskite and Bphen/perovskite interfaces at sufficiently large spike widths and numbers.

Conclusion

The often-overlooked but unique ionotronic conduction in halide perovskites was employed for the demonstration of the comprehensive synaptic signatures that closely emulate biological signal processing. The memristive behaviour was attributed to the co-existence of ion migration and carrier injection barrier in the system, which resulted in self-doping or passivation at the interfaces, and ion relaxation due to the built-in potential in these devices. Presynaptic stimuli first activated short-term plasticity in our artificial synapses and persistent stimuli consolidated the conductance states to achieve long-term plasticity. Delay between the presynaptic and postsynaptic action potentials created temporal correlations in weight changes, resulting in emulation of four forms of spike-timing dependent plasticity rules. Trained as a memory array, these devices depicted reconfigurability and fault tolerance to spurious and random inputs. Network-level simulations of unsupervised learning of handwritten digit images based upon experimentally measured device properties illustrated the power of these memristors for bio-inspired pattern recognition and image classification algorithms. The possibility of exploring the perovskite family of ionic-electronic semiconductors for a novel application with an insight into the desired material characteristics and

conduction mechanism paves way for novel ionotronic neuromorphic architectures with halide perovskites as the active material. Our results motivate a further exploration of the compositional space of perovskites to study the correlation between the material properties and synaptic behaviour. Ruddlesden-Popper (2D) perovskites with bulkier organic ions and incorporation of both 2D and 3D ions within the halide perovskite layer provides the possibility of more exquisite control.[40] Since the interfaces play a significant role in defining the charge injection barriers, investigation of all-inorganic charge extraction layers and ion blockers would enable further insights into the ion migration mechanism under play. The composition of the halide perovskite next to the interface could also be modified to ensure independent ionic/ electronic coupling at the interfaces with respect to the bulk.[41] Demonstration over organic – inorganic hybrid and all-inorganic perovskites raise the appealing prospect that this material system depicts intimate ionic-electronic coupling that can deliver high-performance neuromorphic elements.

Experimental Section:

Device Fabrication. ITO coated glass substrates (7 $\Omega.cm^{-2}$) were cleaned in soap, deionised water, and ethanol solution. Substrates were then subjected to oxygen plasma treatment for 15 minutes, followed by deposition of PEDOT: PSS (the hole transporting layer (HTL)) (Clevios P VP Al 4083) via spin coating (4000 rpm for 60 s). Samples were annealed at 140 °C for 10 minutes in air, after which the perovskite films were spin coated (5000 rpm for 30 s) from equimolar precursor solutions and annealed at 100 °C for 15 minutes under nitrogen environment to remove the solvent residue. Three types of precursor solutions were used, i.e. 1 M CH_3NH_3Br – $PbBr_2$, 1 M $CH(NH_2)_2Br$ – $PbBr_2$ in DMF-DMSO mixture solvent (25 % DMSO), and 0.5 M CsBr – $PbBr_2$ in DMSO solvent. Due to the low solubility of CsBr in the solvent, 0.5 M CsBr and 0.5 M $PbBr_2$ in DMSO solvent was used to deposit $CsPbBr_3$ film instead. In case of MA and FA systems, toluene was dripped for 25 seconds during spin coating to facilitate formation of compact films. 45 nm of bathophenanthroline (Bphen) was then thermally evaporated, followed by evaporation of 7 nm

Calcium and 100 nm aluminum. All evaporation processes were carried out at a base pressure of 4 x 10^{-6} Torr with the active device area defined by shadow masks during calcium and aluminium evaporation. Devices were finally encapsulated using UV-curable epoxy and glass cover.

Characterization. Keithley 2612B was used to record the current density-voltage (J-V) characteristics of the devices. Field emission scanning electron microscopy (FESEM, JEOL JSM-7600F) was employed to characterize the topographical and cross-sectional images, while X-ray diffraction (XRD)-Bruker D8 Advance was used to probe the crystal structure of the films. Electrical measurements were carried out using Keithley 4200-SCS semiconductor characterization system via custom defined pulsing programs.

Supporting Information

Supporting Information is available from the Wiley Online Library or from the author.

Acknowledgements

The authors would like to acknowledge the funding from MOE Tier 1 grant RG 166/16, MOE 2016-T2-1-100 and NRF–CRP14–2014–03. A.B., G.N. and P.K.G. acknowledge MOE Tier 2 grant MOE2013- T2-2-017 for financial support. E.M., D.M. and F.D.A. gratefully acknowledge the project PERSEO- "PERrovskite-based Solar cells: towards high Efficiency and lOng-term stability" (Bando PRIN 2015-Italian Ministry of University and Scientific Research (MIUR) Decreto Direttoriale 4 novembre 2015 n. 2488, project number 20155LECAJ) for funding.

References:

[1] L. F. Abbott, W. G. Regehr, Nature 2004, 431, 796.
[2] G. Indiveri, B. Linares-Barranco, T. J. Hamilton, A. Van Schaik, R. Etienne-Cummings, T. Delbruck, S.-C. Liu, P. Dudek, P. Häfliger, S. Renaud, Front. Neurosci. 2011, 5, 73.
[3] C. Diorio, P. Hasler, A. Minch, C. A. Mead, IEEE Trans. Electron Devices 1996, 43, 1972.
[4] G. Indiveri, E. Chicca, R. Douglas, IEEE Trans. neural networks 2006, 17, 211.
[5] C. Bartolozzi, G. Indiveri, Neural Comput. 2007, 19, 2581.

[6] J. Shi, S. D. Ha, Y. Zhou, F. Schoofs, S. Ramanathan, Nat. Commun. 2013, 4.
[7] R. A. John, F. Liu, N. A. Chien, M. R. Kulkarni, C. Zhu, Q. Fu, A. Basu, Z. Liu, N. Mathews, Adv. Mater. 2018, 1800220.
[8] Z. Wang, S. Joshi, S. E. Savel'ev, H. Jiang, R. Midya, P. Lin, M. Hu, N. Ge, J. P. Strachan, Z. Li, Nat. Mater. 2017, 16, 101.
[9] S. Kim, C. Du, P. Sheridan, W. Ma, S. Choi, W. D. Lu, Nano Lett. 2015, 15, 2203.
[10] R. Yang, H. Huang, Q. Hong, X. Yin, Z. Tan, T. Shi, Y. Zhou, X. Miao, X. Wang, S. Mi, Adv. Funct. Mater. 2018, 28, 1704455.
[11] E. J. Fuller, F. El Gabaly, F. Léonard, S. Agarwal, S. J. Plimpton, R. B. Jacobs-Gedrim, C. D. James, M. J. Marinella, A. A. Talin, Adv. Mater. 2017, 29.
[12] C. Du, W. Ma, T. Chang, P. Sheridan, W. D. Lu, Adv. Funct. Mater. 2015, 25, 4290.
[13] G. Xing, N. Mathews, S. Sun, S. S. Lim, Y. M. Lam, M. Grätzel, S. Mhaisalkar, T. C. Sum, Science (80-.). 2013, 342, 344.
[14] Z. Xiao, Y. Yuan, Y. Shao, Q. Wang, Q. Dong, C. Bi, P. Sharma, A. Gruverman, J. Huang, Nat. Mater. 2015, 14, 193.
[15] Y. Shao, Y. Fang, T. Li, Q. Wang, Q. Dong, Y. Deng, Y. Yuan, H. Wei, M. Wang, A. Gruverman, Energy Environ. Sci. 2016, 9, 1752.
[16] Y. Yuan, J. Huang, Acc. Chem. Res. 2016, 49, 286.
[17] P. C. Harikesh, B. Wu, B. Ghosh, R. A. John, S. Lie, K. Thirumal, L. H. Wong, T. C. Sum, S. Mhaisalkar, N. Mathews, Adv. Mater. 2018, 1802080.
[18] S. A. Veldhuis, P. P. Boix, N. Yantara, M. Li, T. C. Sum, N. Mathews, S. G. Mhaisalkar, Adv. Mater. 2016, 28, 6804.
[19] L. F. Abbott, S. B. Nelson, Nat. Neurosci. 2000, 3, 1178.
[20] S. Wu, K. Y. Wong, M. Tsodyks, Front. Comput. Neurosci. 2013, 7, 188.
[21] P. Feng, W. Xu, Y. Yang, X. Wan, Y. Shi, Q. Wan, J. Zhao, Z. Cui, Adv. Funct. Mater. 2016.
[22] R. A. John, J. Ko, M. R. Kulkarni, N. Tiwari, N. A. Chien, N. Geok, W. L. Leong, N. Mathews, Small 2017, 13.
[23] L. Q. Zhu, C. J. Wan, L. Q. Guo, Y. Shi, Q. Wan, Nat. Commun. 2014, 5.
[24] R. S. Zucker, W. G. Regehr, Annu. Rev. Physiol. 2002, 64, 355.
[25] E. S. Fortune, G. J. Rose, Trends Neurosci. 2001, 24, 381.
[26] T. V Bliss, G. L. Collingridge, Nature 1993, 361, 31.
[27] A. J. Arnold, A. Razavieh, J. R. Nasr, D. S. Schulman, C. M. Eichfeld, S. Das, ACS Nano 2017, 11, 3110.
[28] S. Song, K. D. Miller, L. F. Abbott, Nat. Neurosci. 2000, 3, 919.
[29] V. K. Sangwan, H.-S. Lee, H. Bergeron, I. Balla, M. E. Beck, K.-S. Chen, M. C. Hersam, Nature 2018, 554, 500.
[30] P. U. Diehl, M. Cook, Front. Comput. Neurosci. 2015, 9.
[31] Y. LeCun, C. Cortes, C. J. C. Burges, AT&T Labs [Online]. Available http//yann. lecun. com/exdb/mnist 2010, 2.
[32] M. Oster, R. Douglas, S.-C. Liu, Neural Comput. 2009, 21, 2437.
[33] R. Gopalakrishnan, A. Basu, IEEE Trans. neural networks Learn. Syst. 2017, 28, 778.
[34] S. Brink, S. Nease, P. Hasler, S. Ramakrishnan, R. Wunderlich, A. Basu, B. Degnan, IEEE Trans. Biomed. Circuits Syst. 2013, 7, 71.
[35] J. S. Yun, J. Seidel, J. Kim, A. M. Soufiani, S. Huang, J. Lau, N. J. Jeon, S. Il Seok, M. A. Green, A. Ho-Baillie, Adv. Energy Mater. 2016, 6, 1600330.
[36] J. M. Azpiroz, E. Mosconi, J. Bisquert, F. De Angelis, Energy Environ. Sci. 2015, 8, 2118.
[37] J. Emara, T. Schnier, N. Pourdavoud, T. Riedl, K. Meerholz, S. Olthof, Adv. Mater. 2016, 28, 553.
[38] Y. Zhao, C. Liang, H. min Zhang, D. Li, D. Tian, G. Li, X. Jing, W. Zhang, W. Xiao, Q. Liu, F. Zhang, Z. He, Energy Environ. Sci. 2015, 8, 1256.
[39] Z. Yu, Y. Xia, D. Du, J. Ouyang, ACS Appl. Mater. Interfaces 2016, 8, 11629.

[40] T. M. Koh, K. Thirumal, H. Sen Soo, N. Mathews, ChemSusChem 2016, 9, 2541.
[41] T. M. Koh, V. Shanmugam, X. Guo, S. S. Lim, O. Filonik, E. M. Herzig, P. Müller-Buschbaum, V. Swamy, S. T. Chien, S. G. Mhaisalkar, J. Mater. Chem. A 2018, 6, 2122.

Ionotronic Halide Perovskite Drift-Diffusive Synapses for Low-Power Neuromorphic Computation

Rohit Abraham John[1], Natalia Yantara[2], Yan Fong Ng[1,2], Govind Narasimman[3], Edoardo Mosconi[4,5], Daniele Meggiolaro[4,5], Mohit R. Kulkarni[1], Pradeep Kumar Gopalakrishnan[3], Nguyen Anh Chien[1], Filippo De Angelis[4,5], Subodh G. Mhaisalkar[1,2], Arindam Basu[3], Nripan Mathews[1,2]*

[1] School of Materials Science and Engineering, Nanyang Technological University, 50 Nanyang Avenue, Singapore 639798

[2] Energy Research Institute @ NTU (ERI@N), Nanyang Technological University, 50 Nanyang Drive, Singapore 637553

[3] School of Electrical and Electronic Engineering, Nanyang Technological University, 50 Nanyang Avenue, Singapore 639798

[4] Computational Laboratory for Hybrid/Organic Photovoltaics (CLHYO), CNR-ISTM, Via Elce di Sotto 8, Perugia I-06123, Italy

[5] D3-Computation, Istituto Italiano di Tecnologia, Via Morego 30, 16163 Genova, Italy

*Corresponding author

Prof. Nripan Mathews (Email: Nripan@ntu.edu.sg)

Keywords: Halide Perovskite, Neuromorphic Computing, Synaptic Plasticity, Ionic semiconductor, Ion migration

Section A. Crystal structure of halide perovskites, band diagram of the device stack under test and DC I-V memristive characteristics

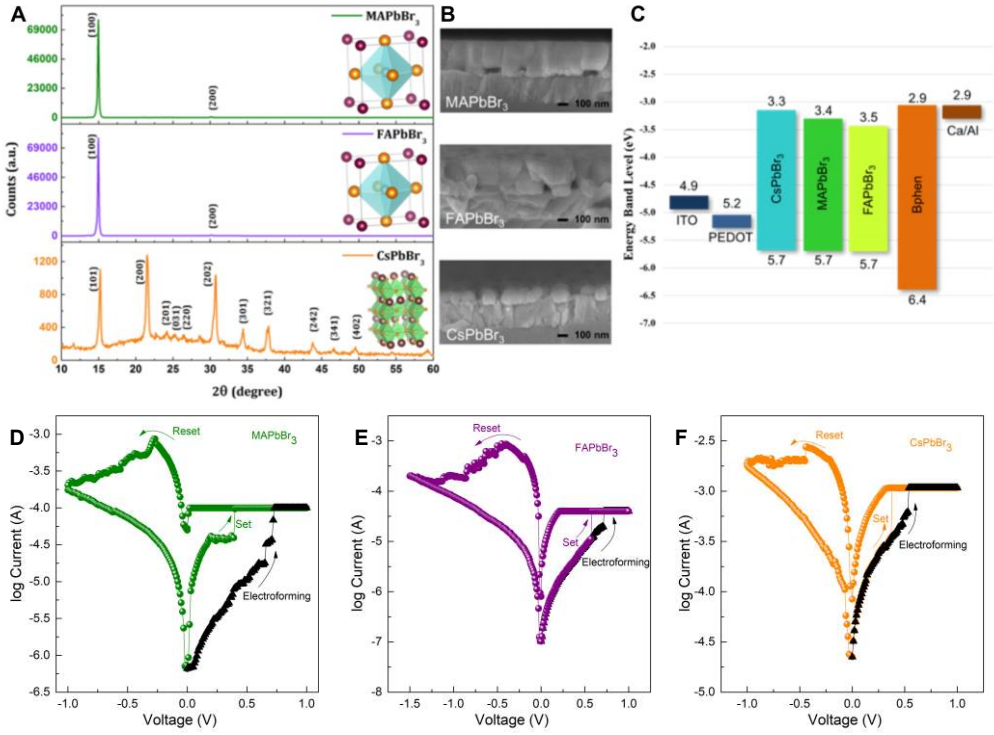

Figure S1. Crystal structure of halide perovskites and their memristive characteristics. (**A**) X-ray diffraction spectra of $MAPbBr_3$, $FAPbBr_3$, and $CsPbBr_3$ films respectively, (**B**) Cross-sectional scanning electron microscope (SEM) images of the halide perovskite films deposited on ITO-PEDOT: PSS. (**C**) Energy band diagram of the device architecture used. (**D-F**) Standard memristor characteristics for $MAPbBr_3$, $FAPbBr_3$ and $CsPbBr_3$- based thin film devices [Device structure: Au/perovskite/ITO].

A series of organic-inorganic halide perovskites (i.e. $MAPbBr_3$, $FAPbBr_3$, and $CsPbBr_3$) were used as active materials for this study. X-ray diffraction spectra of the deposited perovskite films are reported in Figure S1-A. $MAPbBr_3$ and $FAPbBr_3$ films depicted a cubic crystal structure (Pm-3m), while the $CsPbBr_3$ film revealed an orthorhombic crystal structure (Pnma). No additional phase or impurities were observed from XRD spectra of all films. Both $MAPbBr_3$ and $FAPbBr_3$ film were preferentially oriented towards (100) direction. Figure S1-B depicts the cross-sectional scanning electron microscope (SEM) images of the halide perovskite films deposited on ITO-PEDOT: PSS. The memristive devices were built by sandwiching the halide perovskite active layer with hole (HTL) and electron transporting materials (ETL). PEDOT: PSS was utilized as the HTL while Bphen served as the ETL. ITO electrode was used for hole injection while a stack of calcium-

aluminium was employed to inject electrons into the device. The energy band diagram of the corresponding device architecture is shown in Figure S1-C.

Figure S1 D-F shows the DC I-V memristor curves of the active halide perovskite layers [Device structure: Au/perovskite/ITO]. All the 3 active layers demonstrated switching capabilities with a butterfly-like memristor characteristics. Recently, several reports have investigated switching abilities of halide perovskites and have attributed the switching mechanism to vacancy-mediated migration of both halide and A-site cations.[1,2] The switching characteristics of halide perovskites have been reported to heavily depend on the selection of top active electrode, the device area, use of protective oxide/organic layer, etc.[3–6] In this study, we focus on utilizing this memristive/hysteretic property of halide perovskites as a proxy for developing synapses with modulatable plasticity and hence, investigations on factors like top active electrode, the device area, use of protective oxide/organic layer, etc. remain currently out of scope.

Section B. Short-term plasticity (STP)

Chemical synapses exhibit properties of both facilitation and depression, which interact with each other to create short-term plastic changes within neurons according to the dual-process theory of plasticity.[7] When a synapse with low initial probability of vesicle release is stimulated in rapid succession, the second postsynaptic response can be larger than the first - a phenomenon called **neural facilitation or paired-pulse facilitation (PPF)**.[8] In a chemical synapse, temporally correlated action potentials cause voltage-gated Ca^{2+} channels to open, resulting in Ca^{2+} influx and higher presynaptic active calcium (Ca^{2+}) concentration. This in turn triggers synaptic vesicles to release large amounts of neurotransmitters into the synaptic cleft. PPF index, which is the ratio of the amplitude of the second response to that of the first, could be used to quantify facilitation of EPSCs and is an easy measure of synaptic vesicular release probability.[9] PPF is an exclusive presynaptic phenomenon as per the residual Ca^{2+} hypothesis by Katz and Miledi[9], according to

which residual Ca^{2+} after the first impulse causes an increase in neurotransmitter release following the second stimulus. The degree of facilitation is determined by the amount of active Ca^{2+} and is greatest when the Ca^{2+} ions are not allowed to return to the baseline concentration prior to the second stimulus, that is, when the pulse interval is kept shortest. In the opposite scenario, decreased vesicular release probability and inactivation of voltage-gated Ca^{2+} could lead to short-term depression (STD)[9], usually seen in synapses with high probability of initial vesicle release.

Neural-facilitation/PPF contributes to associative learning tasks incorporating auditory-visual signals.[10] Here, PPF was emulated via a pair of programmed presynaptic spikes, which in turn triggered a pair of excitatory postsynaptic currents (EPSCs) analogous to a chemical synapse (Figure S2-A). When the pulse interval between two presynaptic spikes was kept < ~ 50 ms, the PPF index was observed to be much higher than 100 %, indicating strong ionic retention and facilitation at such timescales, akin to the residual Ca^{2+} hypothesis as explained above. For the shortest pulse interval (5.3 ms), MA-based systems depicted the highest PPF index (192%) followed by FA (145%) and Cs (104%), implying different ionic retention capabilities dependent on the active material composition. This ratio continued to decrease with increasing pulse interval and finally reached around 100 % for the largest pulse interval of 2000 ms (Figure 1C). This observed decay resembled the coupling of biological neurons and could be fitted with an exponential decay equation.[11,12]

$$y = B_1 * \exp\left(-\frac{x}{t_1}\right) + B_2 * \exp\left(-\frac{x}{t_2}\right) + y_0$$

where x is pulse interval time, y_0 is resting facilitation magnitude, B_1 & B_2 are facilitation constants, and t_1 and t_2 are characteristic time constants of the rapid and slow phases respectively as shown in Table T1 below.

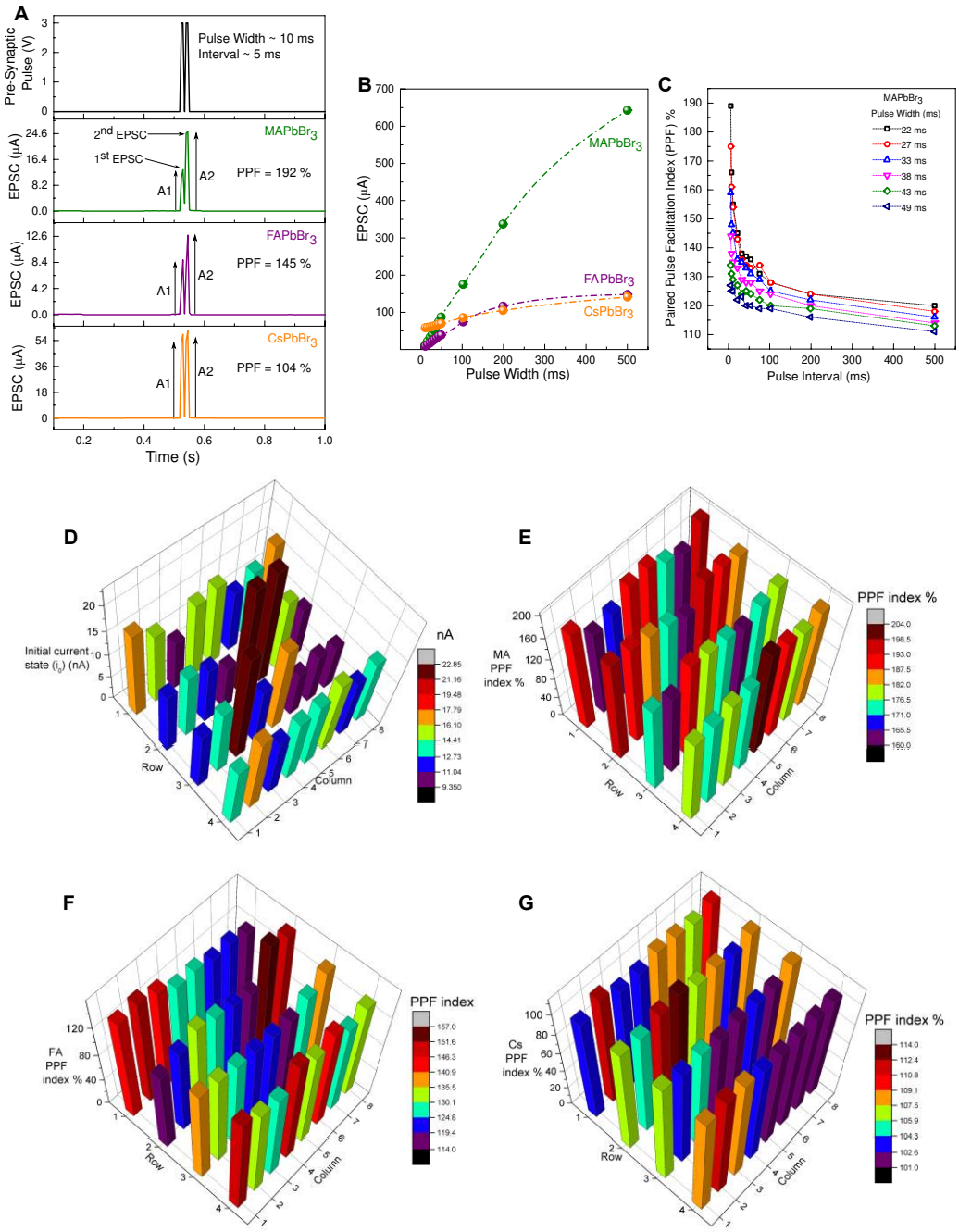

Figure S2. Short-term plasticity in halide perovskite memristors. (**A**) PPF index comparison between $MAPbBr_3$, $FAPbBr_3$ and $CsPbBr_3$. PPF index is defined as the amplitude ratio between the second (A2) and the first (A1) postsynaptic current $[PPF = \left(\frac{A2}{A1}\right) * 100\%)]$.[11] (**B**) Spike-duration-dependent plasticity (SDDP): Postsynaptic current in the artificial synapse as a function of presynaptic spike width. (**C**) PPF index variation with pulse interval of MA devices for increasing pulse widths of presynaptic spikes. Variation in (**D**) EPSCs of $MAPbBr_3$- based devices and PPF indices of (**E**) $MAPbBr_3$, (**F**) $FAPbBr_3$, (**G**) $CsPbBr_3$-based devices fabricated in a single batch consisting of 32 devices.

EPSC and PPF index modulation with pulse interval for increasing pulse widths of presynaptic spikes is depicted in Figures S2-B,C. While larger presynaptic pulse widths induced higher EPSCs

(**Spike-duration-dependent plasticity**), the PPF index reduced inversely. Here, PPF index curves for MA-system is presented for comparison. A maximal PPF index of 192% was obtained for the combination of smallest pulse width and interval of 10.5 ms and 5.3 ms respectively. Although higher pulse width of the prior spike possibly activated a larger number of ions, the depleted ion source for the subsequent second spike could have resulted in the lower effective retention and PPF index. All these modulations of PSCs and short-term indices as a function of the amplitude, number, polarity and frequency of presynaptic spikes, could be utilized as design knobs for implementing bio-inspired temporally-coded algorithms, in congruence with the quantal and stochastic models.[13,14]

Parameter	$MAPbBr_3$	$FAPbBr_3$	$CsPbBr_3$
y_o	103.728	102.22	100.57
B_1	1498.42	194.3	2.4E8
B_2	33.14	25.87	1.75
t_1	1.62	2.28	0.28
t_2	138.92	55.63	57.82
R-Square	0.992	0.993	0.875

Table T1 Best fit values of PPF decay as a function of pulse interval

Figure S2 D-G shows the variation in EPSCs and PPF indices of all the three investigated systems among 32 devices fabricated in a single batch. We would like to point out that the variation in EPSCs was less than 15 nA for MA-based devices as shown in Figure S2-D. FA and Cs-based devices followed a similar trend with Cs showing the least variation among the 3 systems on a general note. Although the PPF indices varied by about 50 % across MA and FA devices (Figure S2 E-F), all the devices depicted an exponentially decaying behaviour with pulse interval, similar to Figure 1C and depicted other short and long-term plasticity features comparable to those demonstrated in this manuscript. Although Cs-based devices depicted the least variability (Figure S2 G), it falls behind in terms of the achievable degree of plasticity.

Section C. Energy consumption

The ON-state energy consumption per spike (Eon) was calculated from the equation[15]

$$E_{on} = I_{peak,first} \times t \times V$$

where $I_{peak,\ first}$ is the maximum value of the 1st generated EPSC for a single spike event, t is the spike duration, and V is the applied voltage. The energy consumption was normalized for an active area of 1 mm^2 for direct comparison with other state-of-the-art reports. We would like to point out that $I_{peak,\ first}$ in the formula for energy calculation is the peak value of current for a single-spike event, i.e. only the magnitude of the 1st EPSC is taken into consideration for calculation (Figure S2-A).[16–19]

A minimum ON-state energy dissipation of 23 nJ/mm^2 per event was obtained for FA-based devices with an active area of 12 mm^2. MA-systems followed closely with a minimum energy dissipation of 34 nJ/mm^2 per event, while Cs-systems drained energy at a minimum rate of 153 nJ/mm^2 per event. All the three systems under investigation depicted energy scaling in a near linear manner across two orders of dimensional magnitude (Figure S3). Hence, with a future scaled version of these devices (1 μm^2), the energy consumption per event could be as low as couple of 10s of fJ/event. Table T2 shows a detailed comparison of the energy consumption our artificial synapses, benchmarked against state-of-the-art reports in literature.

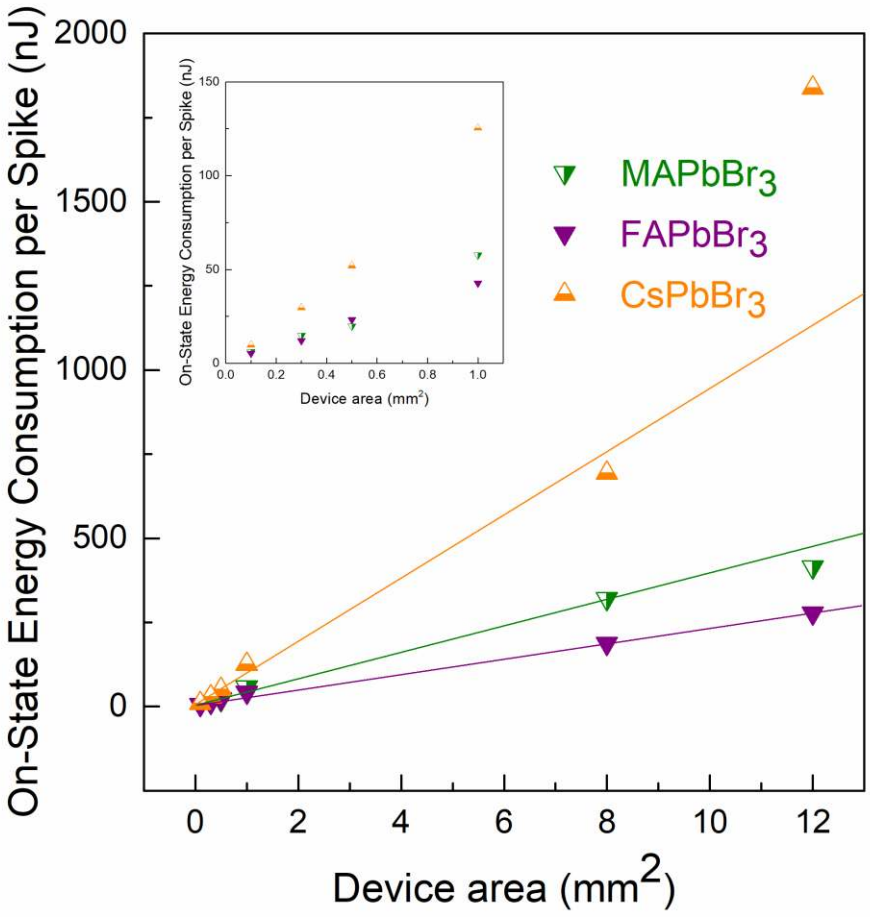

Figure S3. Energy scaling of halide perovskite synapses with device area.

Reference	[4]Xiao et al. *Advanced Electronic Materials* 2.7 (2016): 1600100.	[20]Wang, Yan, et al. *Advanced Materials* (2018): 1802883.	[21]Tian, He, et al. *ACS Nano* 11.12 (2017): 12247-12256.	[22]Shen, Jian-Xin, et al. *Advanced Materials*30.12 (2018): 1706717.	[23]Sun, Linfeng, et al. *Nano Letters* 18. 5 (2018): 3229-3234.	This work
Device	$MAPbI_3$ memristor	$CsPbBr_3$ QD Flash Memory	$(PEA)_2PbBr_4$ memristor	PMN-PT multiferroic heterostructures	MoS_2 device with metal-insulator transition	Halide Perovskite Memristor
Energy Consumption per spike per unit area (nJ/mm^2)	5500	28	400	220	7200	$MAPbBr_3$: 34.5 $FAPbBr_3$: 23 $CsPbBr_3$: 153

Table T2 Comparison of energy consumption of our devices with literature.

Section D. Long-term plasticity

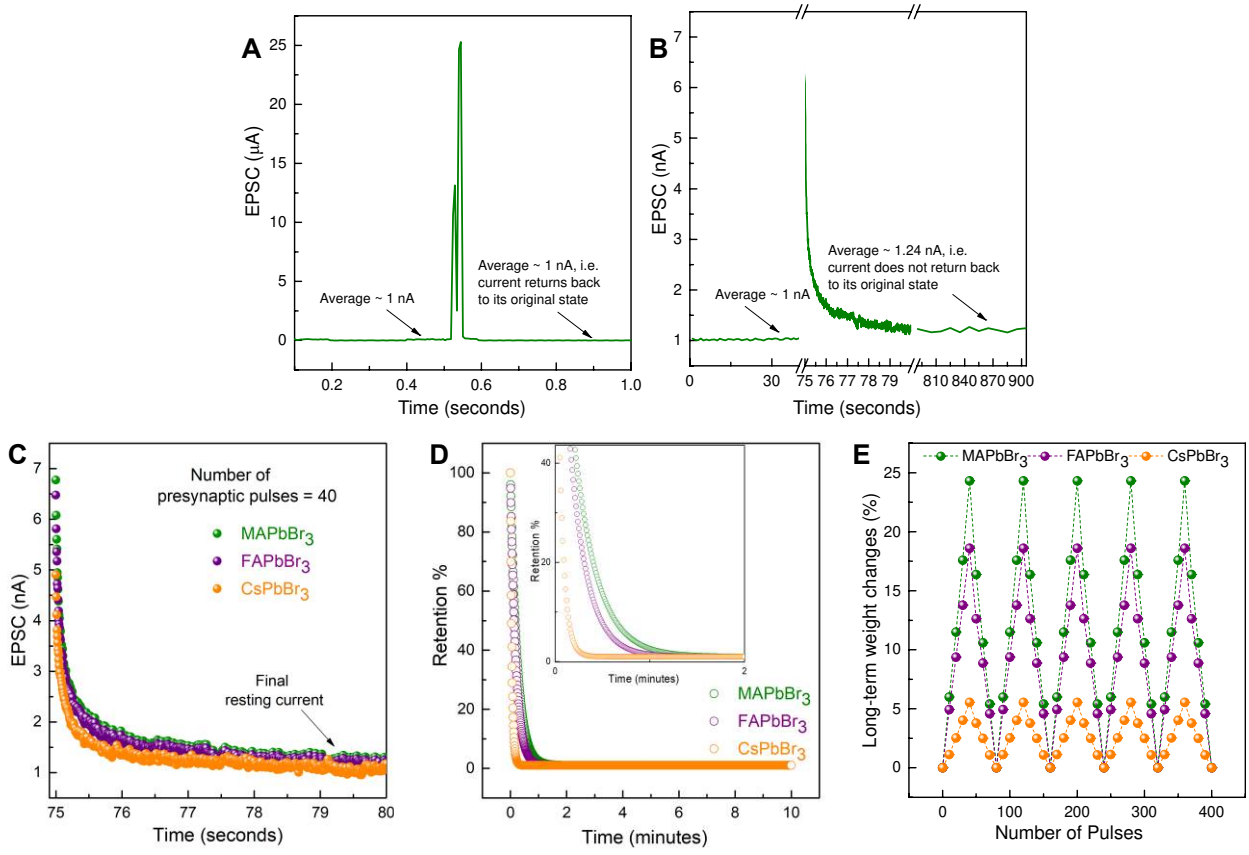

Figure S4. Long-term plasticity in halide perovskite synapses. The metastable conductance-states consolidated to a permanent state on application of > 10 training pulses of width 500 ms and amplitude + 3 V. (**A**) Depicts short-term memory (STM) on application of 2 pulses of amplitude + 3 V, pulse width = 10.5 ms and interval = 5 ms. The current returns back to the original state on removal of the pulse, i.e. volatile change. (**B**) Depicts long-term memory (LTM) on application of 40 pulses of amplitude + 3 V, pulse width = 500 ms and interval = 5 ms. The current does not return back to the original state on removal of the pulse, i.e. non-volatile change. (**A-B**) depicts the STM-LTM transition in our devices. For weight analysis, the conductance state was allowed to reach a stable steady state and the final conductance state was read by a reading pulse of + 0.5 V. Comparison of the long-term potentiation achieved in (**C**) $MAPbBr_3$, $FAPbBr_3$ and $CsPbBr_3$-based synapses trained with 40 pulses of amplitude + 3 V, width 500 ms and interval 5 ms. The graph depicts the decay of current 5 seconds after the application of these pulses. (**D**) The Ebbinghaus forgetting curve depicts the decline of memory retention with time. Highest numerical value of the long-term weight changes were normalized to compare the retention characteristics. Repetitive learning softened the forgetting behaviour. (**E**) Controlled long-term potentiation (LTP) and depression (LTD) were achieved in our devices by applying a series of potentiating and depressing presynaptic spikes. Potentiating spikes were of amplitude + 3 V, while depressing pulses were – 3 V. The degree (slope) of potentiation and depression was dependent on the active material composition and could be further modulated with the amplitude and number of training pulses. Note: Samples with similar initial conductance states were taken for fair analysis.

A form of activity-dependent plasticity which results in a persistent enhancement/weakening of synaptic transmission, **long-term potentiation (LTP)** and **depression (LTD)** satisfies Hebbian criteria as a synaptic memory mechanism. In LTP, excited AMPA receptors cause an influx of Na^+, heavily depolarizing the postsynaptic cell. This EPSP releases Mg^{2+} blocking the NMDA receptor

and allows entry of calcium-glutamate molecules. Increase in intracellular Ca^{2+} activates proteins such as calcium/calmodulin-dependent protein kinase II (CaMKII) and protein kinase C (PKC), facilitating phosphorylation of existing AMPA receptors (AMPAr's) and increasing postsynaptic AMPAr's due to kinase activity. LTP creates changes in both postsynaptic (increased dendritic area and number of AMPA receptors) and presynaptic (increased synaptotagmin levels and total number of presynaptic neurotransmitter vesicles) signalling, thereby enhancing the sensitivity. These changes that occur in both the presynaptic and postsynaptic neurons are the underlying mechanisms for learning and addiction. LTD decreases the efficacy of a synapse due to low frequency stimuli and a slow rise in postsynaptic Ca^{2+}. It has been observed to play a major role in motor learning in the cerebellum, and memory decay in the hippocampus, visual cortex, and prefrontal cortex. Insufficient Ca^{2+} leads to internalization of AMPAr's, decreasing the total sensitivity of the synapse.[24]

LTP and LTD, marked by a permanent increase in synaptic weight were achieved by repeated presynaptic stimulations (analogous to repetitive learning in human brain). In congruence with “the multistore model” of human memory proposed by Atkinson and Shiffrin[25], steep initial facilitation of EPSCs mimicking excitatory glutamatergic systems, and depression emulating inhibitory GABAergic responses were observed in our systems. Transition from a low to high conductance state indicated a time-dependent "consolidation"[26] effect in our devices. For long–term memory measurements, new devices devoid of any history were taken and the initial conductance state was read with a pulse of + 0.5 V. Devices with similar initial conductance states were chosen for a fair analysis. For long-term weight change analysis the following approach has been used in the manuscript throughout:

1. Read the device conductance with V = 0.5 V.

2. Apply necessary voltage waveforms to induce non-volatile weight change/ long-term plasticity. In this manuscript, voltage amplitudes, number and pulse durations have been varied to modulate

this behaviour. For Figures 2 B-D, presynaptic pulses of amplitude + 3 V, width = 500 ms and pulse-interval = 5.3 ms were applied. The number of training pulses were varied to obtain the graphs. For Figures 2 E-G, 40 pulses of width = 500 ms and pulse-interval = 5.3 ms were applied but with varying amplitudes of + 3-5 V.

3. Monitor the channel conductance 15 minutes after application of the waveforms to account for the non-volatile change in conductance and compare it to the initial conductance state to calculate weight %. These stable states observed 15 minutes after application of voltage pulses are the ones taken for analysis of linear weight changes. Table T3 provides a list of the raw initial and final current values used for our analysis.

Material System	$MAPbBr_3$	$FAPbBr_3$	$CsPbBr_3$
Initial current state (nA)	~ 1	~ 1	~ 1
Final current state (nA) after 10 pulses + 3 V	1.0606	1.0506	1.01248
Weight change % after 10 pulses + 3 V	6	5	1
Final current state (nA) after 20 pulses + 3 V	1.115	1.09223	1.02635
Weight change % after 20 pulses + 3 V	11.5	9	2.6
Final current state (nA) after 30 pulses + 3 V	1.1759	1.13847	1.04022
Weight change % after 30 pulses + 3 V	17.6	13.8	4
Final current state (nA) after 40 pulses + 3 V	1.24223	1.18747	1.05409
Weight change % after 40 pulses + 3 V	24	18.7	5.4
Final current state (nA) after 40 pulses + 4 V	1.37769	1.2624	1.08876
Weight change % after 40 pulses + 4 V	37.7	26	9
Final current state (nA) after 40 pulses + 5 V	1.54198	1.33446	1.13037
Weight change % after 40 pulses + 5 V	54	33	13

Table T3 Average values of the current states used for long-term plasticity analysis.

Observation of depression or decrease in conductance was best observed immediately after potentiation measurements and could be induced by applying reverse potential across the device. The degree of potentiation and depression was directly proportional to the total duration and amplitude of pulsing/biasing. Moreover, the rate of such weight changes was dependent on the active material composition as indicated in Figures S4-C-E. Slow relaxation nature of the organic cations resulted in larger weight changes and higher retention of the memory states as depicted by the **Ebbinghaus forgetting curves**. Spaced repetition resulted in softening of the downward slope of the forgetting curve, indicating modulation of the strength of memory and process of forgetting that occurs with the passage of time.

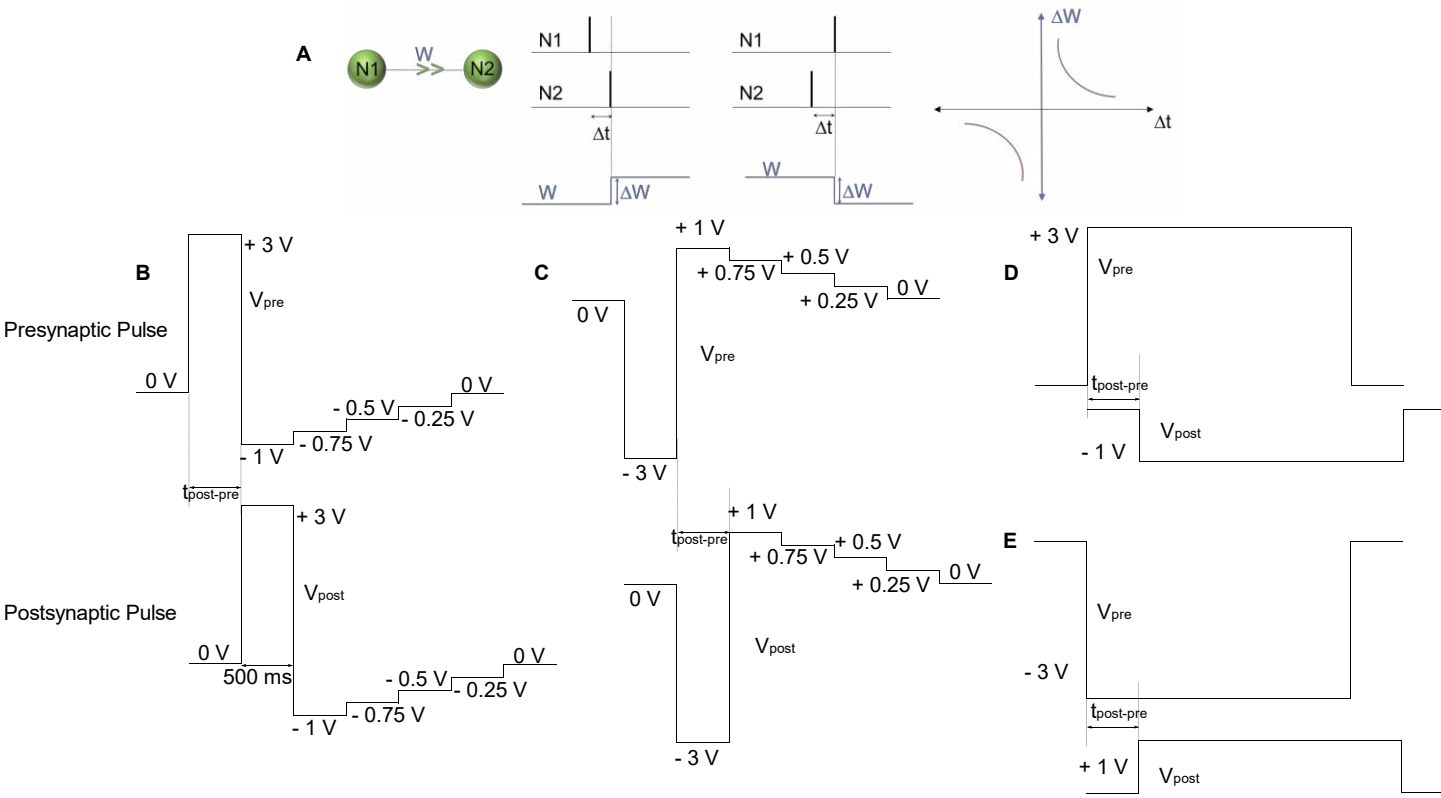

Figure S5. Spike-timing-dependent plasticity (STDP). (A) Difference in timing of the pre- and post-synaptic pulses (Δt) lead to potentiation (pre before post) or depression (post before pre). In circuit realizations, these differences in timing can be translated into voltage amplitude differences in various ways inducing weight changes (ΔW) in the system and hence, facilitating different types of STDP. The graph on the right side shows the commonly observed STDP curves in biology. Input waveforms applied at the pre and post-synaptic terminals to realize (**B**) antisymmetric anti-Hebbian, (**C**) antisymmetric Hebbian, (**D**) symmetric Hebbian, (**E**) symmetric anti-Hebbian learning rules in halide perovskite synapses.

Spike-timing-dependent plasticity (STDP): A refinement of Hebb's theory, STDP is considered to be the first law of synaptic plasticity[27] and forms the basis of associative learning[28] and synfire chain stabilization[29]. In pristine excitatory connections, precedence of presynaptic action potentials results in LTP whereas presynaptic activity following postsynaptic spikes causes long-term depression (LTD) [Antisymmetric Hebbian]. For excitatory to inhibitory connections, LTP and LTD can be induced in the opposite manner [Antisymmetric anti-Hebbian], while in neocortex and neuromuscular junctions, the order does not play a role[27] [Symmetric anti-Hebbian and Hebbian]. The precise relative timing of pre- and postsynaptic spikes significantly affects the sign and magnitude of long-term synaptic modification. Portraying a variety of functional consequences in neural information processing, these different STDP forms reflect the complexity of the underlying cellular mechanisms. Here, spike patterns corresponding to Figure S5 were applied to the pre and

post-synaptic terminals of the halide perovskite synapses, and the change in conductance (weight) was recorded as a function of the pulse interval between pre- and postsynaptic spikes. Four different forms of STDP were realized by modifying the shape of the pre-synaptic and post-synaptic spikes, effectively translating timing differences into voltage amplitude differences (Figures 2H-K). Structurally, the device remained the same. But the resultant weight changes depended on the net effective voltage developed across the device integrated over a time t. For example, when spike pairs corresponding to Figure S5-B was applied to the device at an interval ($t_{post-pre}$) of + 500 ms, the maximum net voltage developed across the device was V_{pre}-V_{post} = (-1) – (+3) = - 4 V. This voltage difference was responsible for the non-volatile weight change and resulted in a decrease in conductance or depression, as evident from right-half of Figure 2H. On arrival of presynaptic pulses after postsynaptic pulses, i.e. $t_{post-pre}$ of - 500 ms, the maximum net voltage developed across the device was V_{pre}-V_{post} = (+ 3) – (- 1) = + 4 V and this resulted in an increase in conductance or facilitation, as evident from the left-half of Figure 2H. Similarly, different voltage waveform shapes applied at the pre- and post-synaptic terminals corresponding to Figures S5 B-E resulted in Figures 2 H-K.

Section E. Simulations on STDP-based unsupervised learning using halide perovskite synapses

A two-layer neural network[30,31] as shown in Figure 3D was used for unsupervised learning of handwritten digits through the interplay of STDP and competition. The input images were converted to spatio-temporal spike patterns by creating a poisson spike train for each pixel with mean firing rate proportional to pixel intensity. Each input was connected to a layer of 400 neurons through excitatory weights (initialized to random values) which were modified by STDP. A second layer of 400 inhibitory neurons induced competition in the network. Each inhibitory neuron was connected to a corresponding excitatory neuron and fired a spike whenever the excitatory neuron fired. Each inhibitory neuron inhibited all excitatory neurons making this a hard winner-take-all

(WTA) circuit. Note that this was done for simplicity in simulations and WTA could be made with a smaller number of inhibitory neurons as well. The equations governing the network dynamics can be broadly divided into the neuronal update and weight update parts. The neuronal update equations governing the membrane potential $V(t)$ are:

$$\tau_{me}\frac{dV}{dt} = (V_{reset} - V) + RI_e$$

$$If\ V(t) > V_{th} + \theta, s(t)\begin{cases} s(t) \to 1, V(t) \to V_{reset} \\ s(t) \to 0 \end{cases}$$

where τ_{me} (membrane time constant) = $100\ ms$, threshold voltage (V_{th}) *of the neuron* = -52 mV, reset voltage (V_{reset}) = -65 mV, $s(t)$ is the spike output of the excitatory neuron, R (leak resistance of the neuron) =10 MΩ and θ is a threshold adaptation parameter that is updated to keep excitation levels of the neurons after learning at a balanced state allowing other neurons to participate in the competition.

I_e denotes the total input current to the excitatory neuron. It can be further decomposed into an excitatory (I_{xe}) and inhibitory (I_{ie}) components as:

$$I_e = I_{xe} + I_{ie}$$

$$I_{xe} = g_{exe}W_{xe}X_{pre}\ , similarly\ I_{ie} = -g_{ie}W_{ie}X_{post}$$

$$\tau_{X_{pre}}\frac{dX_{pre}}{dt} = -X_{pre} + (1 - X_{pre})\sum_{t_i^s}\delta(t - t_i^s)$$

$$\tau_{X_{post}}\frac{dX_{post}}{dt} = -X_{post} + \sum_{t_i^s}\delta(t - t_i^{ex})$$

where X_{pre} is some variable mimicking temporal dynamics of the excitatory postsynaptic current (EPSC) created by excitatory synapses connecting input pixels to layer 1 neurons, W_{xe} denotes corresponding plastic weights normalized to 1 and g_{exe} is a scaling constant. Similarly, X_{post} is the variable for temporal dynamics of the inhibitory PSC created by the synapses connecting layer 2 neurons with layer 1 neurons, W_{ie} denote corresponding fixed weights and g_{ie} is a scaling constant.

Also $\tau_{X_{pre}} = 20\ ms$, $\tau_{X_{post}} = 80\ ms$, t_i^s and t_i^{ex} denote spike times of inputs and excitatory neurons respectively. Finally, the STDP learning equation is applied as follows:

$$\Delta W_{xe}(t_i^{ex}) = \eta(X_{pre}(t_i^{ex}) - X_{tar})(W_{max,xe} - W_{xe})^{\mu}$$

where $\mu = 0.2$, $X_{tar} = 0.4$, $\eta = 0.01$, $W_{max,xe} = 1$.

Here, μ defines the dependence of change in weight on current weight, X_{tar} is the target value of the presynaptic trace at the moment of a postsynaptic spike and η is the learning rate.

To mimic the hardware constraints of the halide perovskite memristor, the maximum weight was bounded to $W_{max,xe}$ and the same voltage waveform X_{pre} was used as the memory trace to govern STDP as well as create the EPSC. Also, the measured STDP window for the halide perovskite synapses was around 2.5 sec; we used a time dilation factor to make the STDP window around 80 ms to speed up simulations. Since all waveforms were equally contracted by the same dilation factor, the dynamics were unchanged. With these settings, the network with 400 excitatory and 400 inhibitory neurons was simulated in MATLAB with 28x28 image inputs from the MNIST database of handwritten digits. The simulation procedure can be summarized as follows:

1. Spike inputs from the image are incident on layer 1 neurons. Each input pixel is connected to all layer 1 neurons.
2. By chance, one of these neurons, say the 20-th neuron in layer 1 (denoted by N^1_{20}), will be maximally excited since its random weights match best with the presented image. It will then fire a spike first. If no neuron fires a spike within the pattern duration, then the same input is again presented to the network but with all input firing rates increased by a constant factor.
3. Once a neuron in layer 1 fires, the corresponding neuron in layer 2 (for the example case above, it is N^2_{20}) will also fire due to high values of connecting weights. Note that each neuron in layer 1 only connects to the corresponding neuron in layer 2.
4. Inhibitory current is then applied to all neurons in layer 1 due to the inhibitory connections from a layer 2 neuron to all layer 1 neurons. This prevents other neurons in layer 1 from firing. Hence, only

weights connecting input to N^1_{20} gets modified by STDP. Weights corresponding to inputs with high firing rate get potentiated while others are depressed.

5. Move to next image and start from step 1.

When the network was presented with 6000 images in a random order and the simulation was run following the steps above, the receptive fields of the excitatory neurons in layer 1 started resembling the input digits through competitive learning as shown in Figure 3D. The major advantage of our proposed halide perovskite based STDP synapse is its low energy consumption during learning. A future miniaturized memristor with an area of 1 μm^2 will consume ~ 23 fJ/weight update (extrapolated from Figure S3). In comparison, memristor based synapses require ~ 30 pJ of write energy[32] while CMOS solutions using floating gate synapses require about 4.5 pJ[31,33]. Compared to other state of the art halide perovskite memristor implementations (Table T2), FA-based memristors depict an 18 % reduction in write energy making them one of the most energy efficient artificial synapses reported till date.

Section F. Galvanostatic measurements

Galvanostatic measurements were done on an Au/Al_2O_3/Perovskite/Al_2O_3/Au device configuration to further evaluate ion-migration within the perovskite active layer alone. For galvanostatic measurement, the symmetric configuration allows electron, hole, and ions to move freely from one electrode to the other (2 directions / linear current-voltage behavior). This is a widely accepted method to prove the existence of ionic migration in perovskites.[34,35] Au strips were thermally evaporated using shadow masks and 2 nm of Al_2O_3 was deposited on top through atomic layer deposition method (ALD). Perovskite layers were then spun coated on top of the sample with a procedure identical to the memristor fabrication to minimize possible differences between the active perovskite layers in both configurations. Upon bias application, positively charged A-cations and negatively charged bromide vacancies drift and accumulate near the negative and positive bias

terminals respectively. The trend in ionic conductivities between $MAPbBr_3$, $FAPbBr_3$, and $CsPbBr_3$ remained consistent with previous observations in the memristor stack, reiterating ion migration in halide perovskites as the plausible explanation for the observed synaptic behavior in our synapses.

In these measurements, voltage and subsequently resistance of device was measured at constant current for a specific period. The total conductivities (σ_{total}) were extracted from the slope (dominated by both electronic (σ_e) and ionic (σ_{ion}, $\sigma_{total} = \sigma_{ion} + \sigma_e$) components) of normal I-V measurements with a scan rate of 4 V/s. In galvanostatic measurements, the measured resistance increased initially and finally saturated with time upon current extraction. At initial stages, resistance was dominated by both electronic and ionic components. The ionic response decreased with time as the ions gradually depleted and accumulated at both electrodes. Finally, the resistance saturated with all the mobile ions blocked at the electrodes, leaving the entire contribution from the electronic component. The electronic component was thus extracted from the resistance at saturation and the ionic counterpart was derived from the difference between total and electronic parts as tabulated in Table T4. The measured conductivities, of the order of 10^{-5} Sm^{-1}, are fully consistent with previous reports on related lead-halide perovskites.[36]

	σ_{ion} (S/m)	σ_e (S/m)	σ_{total} (S/m)
$MAPbBr_3$	8.8×10^{-6}	6.4×10^{-5}	7.2×10^{-5}
$FAPbBr_3$	8.3×10^{-6}	6.3×10^{-5}	7.1×10^{-5}
$CsPbBr_3$	6.1×10^{-6}	1.1×10^{-5}	1.7×10^{-5}

Table T4. The calculated ionic, electronic, and total conductivities of halide perovskite thin films with different cations.

Section G. Ionic migration model and first principles calculations

Model and first-principles calculations. First principles calculations on $MAPbBr_3$, $FAPbBr_3$ and $CsPbBr_3$ were performed on their room-temperature stable phases (pseudo-cubic and orthorhombic, respectively) (Table T5). The reported geometries are those of the transition states along each

pathway. The yellow circles represent the initial and final ionic positions, with blue arrows indicating the migration pathway. (Atomic color codes: Purple: Cs; Red: Br; Light blue: Pb; Green: C; Blue: N; White: H.) (Figure 4D). These calculations indicated that vacancy-mediated migration activation energies of both halide and A-site cations (i.e. MA, FA and Cs) were considerably lower than those for Pb^{2+} migration. Halide motion is predicted to be observable on a very short timescale (< 1 μs) due to its small migration activation energy (~ 0.1 eV for the three compounds). These timescales and comparable activation energies do not match the experimental phenomena presented here. On the other hand, significant differences in activation energy for A-site cation migration through the corresponding vacancies (V_{MA-}: 0.56 eV, V_{FA-}: 0.61 eV, and V_{Cs-}: 0.32 eV) which can take place on a time scale of ~ ms to minutes, could be the origin of the transient responses noted here.[37] Our calculations on lead-bromide perovskites are consistent with results for lead-iodide compounds showing similar activation energies for MA and FA vacancy migration.[38] The strong differences between organic (FA≈MA) and inorganic (Cs) vacancy-mediated migration activation energy is consistent with the cation size order (FA>MA >> Cs). Although both halide and cations are easy to diffuse, the synaptic behaviour in our study is heavily influenced by the cation movement due to the long pulse widths (~ ms) employed here.

E_a	$MAPbBr_3$	$FAPbBr_3$	$CsPbBr_3$
V_{Br+}	0.09	0.12	0.13
$V_{MA-/FA-/Cs-}$	0.56	0.61	0.32
V_{Pb--}	1.51		

Table T5. Calculated vacancy migration energy barriers (eV) for $MAPbBr_3$, $FAPbBr_3$ and $CsPbBr_3$ using the experimental cell parameters.

The migration energy barriers remained similar when simultaneously optimizing the atomic coordinates and cell parameters. For V_{MA} (V_{FA}), the migration energy barriers of 0.56 (0.61 eV) at fixed cell parameters became 0.46 (0.61 eV) when allowing the cell parameters to optimize. Unfortunately, Cs-based systems did not converge on a reasonable TS structure when allowing cell relaxation.

The formation of A-cation vacancies on the representative $CsPbBr_3$ and $MAPbBr_3$ compounds was further investigated. We checked several different levels of theory and applied different corrections to charged species, but in any case, the results always showed a comparable (i.e. within less than 0.1 eV see Table T6) defect formation energy (DFE) for V_{MA} and V_{Cs}. Thus, we believe the leading factor in determining the different behaviour of the various A-cations is their migration energy barrier, with the possibly different DFE representing a fine-tuning contribution.

no vdW	**DFE (E_f=0, eV)**
V_{MA}^-	-0.25
V_{Cs}^-	-0.27
Br-rich	
vdW	**DFE (E_f=0, eV)**
	eq_$PbBr_2$
V_{MA}^-	0.1
V_{Cs}^-	0.06

Table T6. Calculated defect formation energies (DFE) for A-cation vacancies.

Computational Details. Density Functional Theory (DFT) calculations were carried out, within a plane wave/pseudopotential approach, as implemented in the PWSCF program of the Quantum Espresso software package.[39] To accommodate the different point defects studied and their migration along the perovskite crystal, a rather large tetragonal unit cell containing 384 atoms (32 PbI_3 units) was built up. The PBE[40] exchange-correlation functional was used along with ultra-soft, scalar relativistic pseudopotentials for all atoms. Plane wave cut-offs of 25 and 200 Ry were adopted for expansion of the wave function and density respectively, sampling the first Brillouin zone at the Γ point only. Electron−ion interactions were described by ultra-soft pseudopotentials with electrons from N, C 2s2p, H 1s, Pb 6s6p5d, Br 4s4p and Cs 5s5p6s electrons explicitly included in the calculations. Structural optimizations were performed with cell parameters fixed to the experimental values reported by Poglitsch and Weber.[41] The scalar relativistic approach (SR) for structural optimizations was adopted, since spin-orbit coupling is known to play a minor role on

the structure. Linear transit calculations were performed to calculate the energy profile along the migration paths of the defects, identify the saddle point, and estimate the energy barriers.

References:

[1] W. Tress, J. Phys. Chem. Lett. 2017, 8, 3106.
[2] J. Choi, S. Park, J. Lee, K. Hong, D. Kim, C. W. Moon, G. Do Park, J. Suh, J. Hwang, S. Y. Kim, Adv. Mater. 2016, 28, 6562.
[3] D. Liu, Q. Lin, Z. Zang, M. Wang, P. Wangyang, X. Tang, M. Zhou, W. Hu, ACS Appl. Mater. Interfaces 2017, 9, 6171.
[4] Z. Xiao, J. Huang, Adv. Electron. Mater. 2016, 2.
[5] K. Yan, M. Peng, X. Yu, X. Cai, S. Chen, H. Hu, B. Chen, X. Gao, B. Dong, D. Zou, J. Mater. Chem. C 2016, 4, 1375.
[6] W. Xu, H. Cho, Y. Kim, Y. Kim, C. Wolf, C. Park, T. Lee, Adv. Mater. 2016, 28, 5916.
[7] R. S. Zucker, Annu. Rev. Neurosci. 1989, 12, 13.
[8] N. P. Vyleta, P. Jonas, Science (80-.). 2014, 343, 665.
[9] S. L. Jackman, J. Turecek, J. E. Belinsky, W. G. Regehr, Nature 2016, 529, 88.
[10] J. C. López, Nat. Rev. Neurosci. 2001, 2, 307.
[11] R. A. John, J. Ko, M. R. Kulkarni, N. Tiwari, N. A. Chien, N. Geok, W. L. Leong, N. Mathews, Small 2017, 13.
[12] P. Feng, W. Xu, Y. Yang, X. Wan, Y. Shi, Q. Wan, J. Zhao, Z. Cui, Adv. Funct. Mater. 2016.
[13] T. C. Sudhof, Annu. Rev. Neurosci. 2004, 27, 509.
[14] J. Del Castillo, B. Katz, J. Physiol. 1954, 124, 560.
[15] A. M. Shen, C.-L. Chen, K. Kim, B. Cho, A. Tudor, Y. Chen, ACS Nano 2013, 7, 6117.
[16] C. Sen Yang, D. S. Shang, N. Liu, G. Shi, X. Shen, R. C. Yu, Y. Q. Li, Y. Sun, Adv. Mater. 2017, 29, 1700906.
[17] J. Yang, C. Ge, J. Du, H. Huang, M. He, C. Wang, H. Lu, G. Yang, K. Jin, Adv. Mater. 2018, 1801548.
[18] W. Xu, T. L. Nguyen, Y.-T. Kim, C. Wolf, R. Pfattner, J. Lopez, B.-G. Chae, S.-I. Kim, M. Y. Lee, E.-Y. Shin, Nano Energy 2018, 48, 575.
[19] J. Zhu, Y. Yang, R. Jia, Z. Liang, W. Zhu, Z. U. Rehman, L. Bao, X. Zhang, Y. Cai, L. Song, Adv. Mater. 2018, 30, 1800195.
[20] Y. Wang, Z. Lv, J. Chen, Z. Wang, Y. Zhou, L. Zhou, X. Chen, S. Han, Adv. Mater. 2018, 1802883.
[21] H. Tian, L. Zhao, X. Wang, Y.-W. Yeh, N. Yao, B. P. Rand, T.-L. Ren, ACS Nano 2017, 11, 12247.
[22] J. Shen, D. Shang, Y. Chai, S. Wang, B. Shen, Y. Sun, Adv. Mater. 2018, 30, 1706717.
[23] L. Sun, Y. Zhang, G. Hwang, J. Jiang, D. Kim, Y. A. Eshete, R. Zhao, H. Yang, Nano Lett. 2018, 18, 3229.
[24] M. F. Bear, R. C. Malenka, Curr. Opin. Neurobiol. 1994, 4, 389.
[25] T. Ohno, T. Hasegawa, T. Tsuruoka, K. Terabe, J. K. Gimzewski, M. Aono, Nat. Mater. 2011, 10, 591.
[26] T. V Bliss, G. L. Collingridge, Nature 1993, 361, 31.
[27] Y. Li, Y. Zhong, L. Xu, J. Zhang, X. Xu, H. Sun, X. Miao, Sci. Rep. 2013, 3.
[28] P. D'Souza, S.-C. Liu, R. H. R. Hahnloser, Proc. Natl. Acad. Sci. 2010, 107, 4722.
[29] A. Waddington, P. A. Appleby, M. De Kamps, N. Cohen, Front. Comput. Neurosci. 2012, 6.
[30] P. U. Diehl, M. Cook, Front. Comput. Neurosci. 2015, 9.
[31] R. Gopalakrishnan, A. Basu, IEEE Trans. neural networks Learn. Syst. 2017, 28, 778.

[32] S. H. Jo, T. Chang, I. Ebong, B. B. Bhadviya, P. Mazumder, W. Lu, Nano Lett. 2010, 10, 1297.
[33] S. Brink, S. Nease, P. Hasler, S. Ramakrishnan, R. Wunderlich, A. Basu, B. Degnan, IEEE Trans. Biomed. Circuits Syst. 2013, 7, 71.
[34] Y. Shao, Y. Fang, T. Li, Q. Wang, Q. Dong, Y. Deng, Y. Yuan, H. Wei, M. Wang, A. Gruverman, Energy Environ. Sci. 2016, 9, 1752.
[35] T. Y. Yang, G. Gregori, N. Pellet, M. Gr??tzel, J. Maier, Angew. Chemie - Int. Ed. 2015, 54, 7905.
[36] A. Senocrate, I. Moudrakovski, G. Y. Kim, T. Yang, G. Gregori, M. Grätzel, J. Maier, Angew. Chemie Int. Ed. 2017, 56, 7755.
[37] J. M. Azpiroz, E. Mosconi, J. Bisquert, F. De Angelis, Energy Environ. Sci. 2015, 8, 2118.
[38] J. Haruyama, K. Sodeyama, L. Han, Y. Tateyama, J. Am. Chem. Soc. 2015, 137, 10048.
[39] P. Giannozzi, S. Baroni, N. Bonini, M. Calandra, R. Car, C. Cavazzoni, D. Ceresoli, G. L. Chiarotti, M. Cococcioni, I. Dabo, J. Phys. Condens. matter 2009, 21, 395502.
[40] J. P. Perdew, K. Burke, M. Ernzerhof, Phys. Rev. Lett. 1996, 77, 3865.
[41] A. Poglitsch, D. Weber, J. Chem. Phys. 1987, 87, 6373.